



Shear-induced crystallization of polyamide 11

Katalee Jariyavidyanont¹ · Salvatore Mallardo² · Pierfrancesco Cerruti² · Maria Laura Di Lorenzo² · Regine Boldt³ · Alicyn M. Rhoades⁴ · René Androsch¹

Received: 14 December 2020 / Revised: 4 February 2021 / Accepted: 20 February 2021 / Published online: 18 March 2021
© The Author(s) 2021

Abstract

Shear-induced formation of crystal nuclei in polyamide 11 (PA 11) was studied using a conventional parallel-plate rheometer. Crystallization of PA 11 after shearing the melt at different rates for 60 s was followed by the evolution of the complex viscosity. The sheared samples showed in an optical microscope a gradient structure along the radius, due to the increasing shear rate from the center to the edge. The critical shear rate for shear-induced formation of nuclei was identified at the position where a distinct change of the semicrystalline superstructure is observed, being at around 1 to 2 s^{-1} . Below this threshold, a space-filled spherulitic superstructure developed as in quiescent-melt crystallization. Above this value, after shearing at rates between 1 and 5 s^{-1} , an increased number of point-like nuclei was detected, connected with formation of randomly oriented crystals. Shearing the melt at even higher rates led to a further increase of the nuclei number and growth of crystals oriented such that the chain axis is in parallel to the direction of flow. In addition, optical microscopy confirmed formation of long fibrillar structures after shearing at such condition. The critical specific work of flow of PA 11 was calculated to allow a comparison with that of polyamide 66 (PA 66). This comparison showed that in the case of PA 11 more work for shear-induced formation of nuclei is needed than in the case of PA 66, discussed in terms of the chemical structure of the repeat unit in the chains.

Keywords Polyamide 11 · Shear-induced nucleation/crystallization · Crystallization · Specific work of flow · Semicrystalline morphology

Introduction

Polyamide 11 (PA 11), produced by Arkema (trade name Rilsan[®]), is a bio-based polymer which is synthesized by polycondensation of ω -aminoundecanoic acid, extracted from castor oil (Genas 1962). It is an aliphatic polyamide

with its repeating unit consisting of a rather long sequence of ten methylene groups and an amide group. PA 11 is a crystallizable polymer exhibiting a rather low maximum crystallinity of less than 40% (Zhang et al. 2000). Due to its good chemical resistance, excellent impact properties, and good dimensional stability, it is considered a high-performance engineering polymer used in versatile applications such as automotive components, on-shore and off-shore oil pipelines, electronic components, gears, connectors, coating material, and diverse medical applications (Kohan 1995; Bello and Wood 2005; Halim et al. 2013). The properties, tailored for each of those applications, strongly depend on the semicrystalline structure, including fraction, size, shape, orientation, and perfection of crystals (Tordjeman et al. 2001; Azzurri et al. 2003; Dencheva et al. 2007; Kolesov et al. 2014). These parameters, in turn, are controlled by the crystallization and processing conditions (Jariyavidyanont et al. 2019).

Regarding quiescent-melt crystallization of PA 11 at processing-relevant cooling rates, the melt completely vitrifies

✉ Katalee Jariyavidyanont
katalee.jariyavidyanont@iw.uni-halle.de

✉ René Androsch
rene.androsch@iw.uni-halle.de

¹ Interdisciplinary Center for Transfer-oriented Research in Natural Sciences, Martin Luther University Halle-Wittenberg, 06099 Halle/Saale, Germany

² Institute of Polymers, Composites and Biomaterials (CNR), Via Campi Flegrei, 34, 80078 Pozzuoli, Naples, Italy

³ Leibniz-Institut für Polymerforschung Dresden e.V., Hohe Str. 6, 01069 Dresden, Germany

⁴ School of Engineering, Penn State Behrend, 4701 College Drive, Erie, PA 16563, USA

below the glass transition temperature (T_g) of about 45 °C on quenching at rates faster than about 1000 K s⁻¹ (Mollova et al. 2013; Jariyavidyanont et al. 2019), while cooling at lower rates allows crystallization/ordering. Formation of mesomorphic pseudohexagonal δ' -crystals is obtained at high supercooling of the melt slightly above T_g on cooling at rates between 200 and 500 K s⁻¹ (Schmidt and Stuart 1958; Rhoades et al. 2016). At such conditions, many crystal nuclei are active, hindering their lateral growth to lamellae and formation of spherulites. Instead, small ordered domains/nodules develop (Mollova et al. 2013; Schick and Androsch 2018). Cooling slower than 200 K s⁻¹ increasingly leads to high-temperature spherulitic crystallization of the melt, replacing the low-temperature ordering process. Finally, cooling at rates lower than 30 K s⁻¹ permits for the formation of a space-filled spherulitic structure by the growth of few nuclei at high temperature to lamellar pseudohexagonal δ -crystals (Mollova et al. 2013; Jariyavidyanont et al. 2019). These crystals convert reversibly on cooling to ambient temperature to triclinic α -crystals at the Brill-transition temperature at around 100 °C (Brill 1942; Pepin et al. 2016).

In polymer-manufacturing processes, crystallization often takes place in a non-quiescent highly supercooled melt due to high cooling rates and simultaneous presence of normal and shear forces/stress, causing deformation and/or orientation of the molecules (Somani et al. 2005; Ogino et al. 2006). Crystallization of PA 11 during injection molding and the resulting semicrystalline morphology were analyzed and correlated to the cooling-rate profile in the various regions of the molded part (Jariyavidyanont et al. 2018). Fast cooling at a rate of few hundred K s⁻¹ was predicted in the skin layer by simulation, and optical microscopy and X-ray analysis revealed formation of non-spherulitically grown α -crystals of low perfection. Toward the core, with increasing distance from the skin, the cooling rate decreased, allowing for formation of a spherulitic structure containing more perfect α -crystals.

An intermediate zone between the skin and core regions, often called a shear zone, is generally observed as a result of shearing the melt during the filling process. Shear rates of the order of magnitude of 10³ s⁻¹ may be evident for a short period of time of around 1 s before crystallization, as simulated for a specific molding of isotactic polypropylene (Gohn et al. 2018). As a consequence, nucleation and crystallization are enhanced, as detected by an increase of the nuclei density, leading to a fine-spherulitic or non-spherulitic structure (Koscher and Fulchiron 2002; Janeschitz-Kriegl et al. 2003; Pantani et al. 2010; De Santis et al. 2016; Spoerer et al. 2020), due to the lower energy barrier for the formation of crystal nuclei (Coppola et al. 2001; Koscher and Fulchiron 2002; Lellinger et al. 2003). If the shear flow is strong enough (Hadinata et al. 2006; Mykhaylyk et al.

2008; Seo et al. 2018; Refaa et al. 2018; Iqbal et al. 2019), even oriented superstructures may form, like shish-kebab morphologies or aligned spherulites (Keller and Machin 1967; Zhang et al. 2005).

Regarding quantitative data on shear-induced crystallization of PA 11, we are aware of only a single study performed on branched molecules (Acierno and Puyvelde 2005). As far as we know, there exists no information about critical shearing conditions of PA 11 to promote shear-induced formation of nuclei, therefore being subject of the present work. Crystallization of PA 11 is followed via evolution of the complex viscosity collected during isothermal crystallization after shearing the melt at different rates, using a parallel-plate rheometer. The critical shear rate, defined as minimum shear rate applied to the sample to induce/enhance crystallization, was investigated and, after its compilation into a specific work of flow (W), compared with results of a similar study performed on polyamide 66 (PA 66) (Seo et al. 2018). The specific work of flow (Janeschitz-Kriegl et al. 2003) is calculated according to Eq. 1 and considers besides the shear rate ($\dot{\gamma}$) also the effects of shear time (t) and viscosity of the melt (η), depending on temperature and time of shear, on nuclei formation:

$$W = \int_{t_0}^{t_s} \eta(T, t) \dot{\gamma}^2 dt \quad (1)$$

Furthermore, besides correlating the shearing conditions with the kinetics of crystallization/nuclei formation, structural data including degree of crystallinity, crystal structure, and micrometer-scale superstructure were analyzed using differential scanning calorimetry (DSC), wide-angle X-ray scattering (WAXS), and polarized-light optical microscopy (POM), for interpretation of the effect of shear-induced crystallization on structure.

Experimental

Material and preparation

High-viscosity bio-based Rilsan[®] BESNO-TL PA 11, an extrusion grade containing heat and light stabilizers, was obtained from Arkema. The melt volume-flow rate, mass-average molar mass, and polydispersity are 1 cm³ (10 min)⁻¹ (235 °C, 2.16 kg) (Arkema 2020), 17.2 kg mol⁻¹, and 2, respectively (Fornes and Paul 2004). The material, delivered in the form of pellets, was dried at 80 °C for about 12 h before film compression molding. A pre-pressed film with a thickness of about 800 μ m was prepared by a Carver laboratory manual press at 220 °C using a maximum load of 2 t and then cut to obtain a circular disk with a diameter of about 16 mm for subsequent rheological analysis.

Rheological analysis

Shear-induced crystallization of PA 11 was investigated by using a Thermo Scientific HAAKE Rheostress6000 rheometer equipped with a closed temperature-controlled chamber and a 20-mm-diameter parallel-plate geometry setup. The chamber, purged with nitrogen gas at 20 mL min^{-1} , was heated to $220 \text{ }^\circ\text{C}$, equilibrated at this temperature for a few minutes, before adjusting the position of the upper shaft/plate by zero-gap setting. A 16-mm-diameter sample disk with a thickness of about $800 \text{ }\mu\text{m}$ was placed between the metal plates and equilibrated at $220 \text{ }^\circ\text{C}$ for 1 min. After that, the upper metal-plate was slowly lowered to the pre-defined gap distance of $500 \text{ }\mu\text{m}$, and the excess melt was trimmed from the outer edges of the plates. Note that the selected gap distance of $500 \text{ }\mu\text{m}$ was set according to the ISO 6721-10 standard, with the recommendation of the ratio $2r/h$ to be between 10 and 50 (r and h are the radius and gap distance, respectively) (Mezger 2006). Otherwise, if it is outside of the recommended range, there is risk of inhomogeneous deformation, secondary flow effects, transient behavior, and edge failure.

The shear and crystallization experiments were performed according to the protocol shown in Fig. 1. After trimming, the melt was kept at $220 \text{ }^\circ\text{C}$ for additional 2 min and then ballistically cooled at a rate of about $15\text{--}20 \text{ K min}^{-1}$ to the shear temperature of $190 \text{ }^\circ\text{C}$. Different shear rates, up to 10 s^{-1} , were applied to the sample for 60 s in all experiments. Note that the shear rate depends on the location in the disk, linearly increasing with the radius (Mezger 2006). In the following, shear rate information refers to the maximum shear rate at the edge of the plate ($r = 10 \text{ mm}$). After the shear step, the sample was cooled at a rate of 10 K min^{-1} to $180 \text{ }^\circ\text{C}$ and isothermally crystallized at this temperature for 1 h, allowing for completion of primary crystallization. The crystallization kinetics was monitored by the time dependence

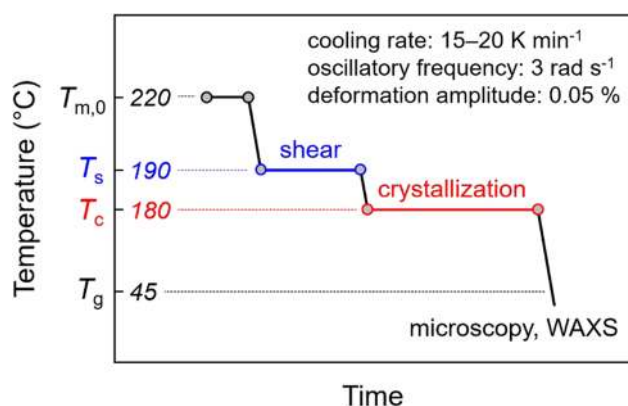


Fig. 1 Temperature and shear protocol for analysis of shear-induced crystallization of PA 11

of the complex viscosity, measured using an oscillatory frequency and deformation amplitude of 3 rad s^{-1} and 0.05% , respectively. For morphological and crystallinity analyses, Kapton[®] polyimide films, used as a non-adhesive layer, were glued on both metal plates before zero-gap setting. Shear and crystallization experiments for a given shear condition typically were performed at least two times (often up to four times) when using Kapton, being the preferred setup since allowing subsequent structure analysis. Since there was often observed a difference between program shear rate and true shear rate, error bars could not be obtained rather than an increased number of different shear-rate data. Experiments without using Kapton were performed only once, just for comparison with data obtained using Kapton-setup.

Differential scanning calorimetry

DSC was employed to investigate the crystallinity of a non-sheared sample and a sample crystallized after shearing the melt at a rate of about 7.6 s^{-1} . The samples with a mass of $5\text{--}10 \text{ mg}$ were taken near the center and edge of the disks and subsequently placed into $20 \text{ }\mu\text{L}$ aluminum pans. A heat-flux Mettler-Toledo DSC 1 in combination with a TC100 intracooler was used. The furnace was purged with nitrogen gas at a flow rate of 60 mL min^{-1} . The calibration of the instrument was checked by measurement of the temperature and enthalpy of melting of an indium standard. The crystallinity was estimated from the enthalpy of melting during heating using a rate of 20 K min^{-1} , with its calculation based on a value of the bulk enthalpy of melting of 189 J g^{-1} (Zhang et al. 2000).

Polarized-light optical microscopy

The microstructure of non-sheared and sheared PA 11, after completion of the crystallization step and cooling to room temperature, was analyzed by POM. Thin sections with a thickness of about $10 \text{ }\mu\text{m}$ were prepared using a SLEE-CUT-5062 rotary microtome. The sections were cut along the radius of the disks, from the center through the edge, that is, perpendicular to the flow direction. Then, thin sections were embedded in immersion oil between glass coverslips and observed with a Leica DMRX optical microscope in transmission mode using crossed polarizers. The images were captured by a Motic 2300 CCD camera attached to the microscope.

Wide-angle X-ray scattering

WAXS was used to investigate the crystal structure and orientation as a function of the radial position in the disks from the edge to the center. The analysis was performed at room temperature in transmission mode employing a Bruker D8

Discover X-ray diffractometer, equipped with an area detector, and using Cu K_{α} radiation. The diameter of the circular beam was 0.5 mm and the exposure time was 30 min. The sample-to-detector distance was 149.7 mm.

Results and discussion

Figure 2 shows the evolution of the complex viscosity of PA 11 collected during isothermal crystallization at 180 °C for 1 h (see the red segment in Fig. 1). The data of the upper plot were obtained from the samples placed between the metal plates without using Kapton® films. The shear rates, as given in the legend, represent average values over the total shear time of 60 s. The bottom sets of data were obtained from the experiments using Kapton® films. In this case, the onset time of crystallization/increase of the viscosity is slightly delayed if compared to the data observed in experiments without using Kapton® (top data), as described below. Furthermore, in the lower plot, the upper plateau of the viscosity curves is not shown due to lack of reproducibility when samples exhibit high viscosity due to presence of crystals, in case of using Kapton® film. However, crystallization onset times are reproducible, since at this stage of the crystallization step, the viscosity is low, not leading to detrimental effects

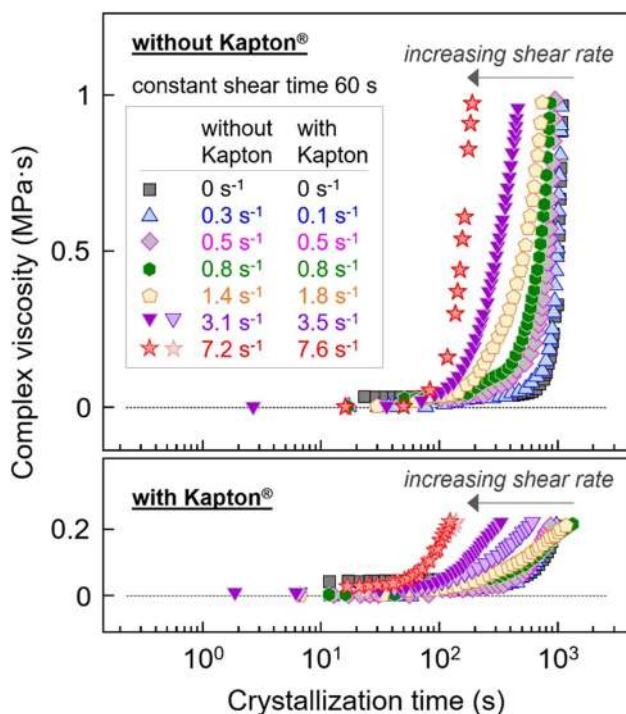


Fig. 2 Viscosity as a function of crystallization time of PA 11 obtained during isothermal crystallization at 180 °C, after shearing the melt at different rates for 60 s. The data of the lower plot were collected using Kapton® films for easy removal of the sample from the instrument after crystallization

of the Kapton® films. Quiescent-melt crystallization of the samples, regardless of the use of Kapton® films, begins after about 1000 s (see black squares), being in agreement with former DSC studies of the crystallization rate (Mollova et al. 2013; Rhoades et al. 2016). When shearing the melt, crystallization shifts to increasingly shorter time with increasing shear rate (see gray arrows), caused by an increase of nuclei density.

Figure 3 shows crystallization onset times as a function of shear rate of PA 11, with black squares and red stars referring to data measured either with or without Kapton®, respectively. Crystallization onset times are defined as intersection of the extrapolated baseline and the estimated highest-slope tangent line of the viscosity curves of Fig. 2. The onset times of crystallization of non-sheared samples are indicated with the corresponding black and red dashed lines, respectively. Regarding non-sheared samples, we observed a slightly lower onset time of crystallization when using Kapton®. In detail, in case of not using Kapton® as a spacer/anti-adhesive, the onset time of crystallization is about 1050 s, while it is about 950 s when using Kapton®, perhaps caused by a nucleating effect of the Kapton® film (Gadzinowska and Piorkowska 2003). The trend of slightly faster crystallization in case of the Kapton®-setup seems to be preserved also in experiments in which samples are subjected to shear despite occasional uncertainties in determination of the crystallization onset time. However, the observed negligible difference of the crystallization rate in case of the two experimental setups has no influence on the discussion of the effect of shear on crystallization.

In fact, regardless of the use of Kapton® films, the crystallization time distinctly decreases on shearing the melt at

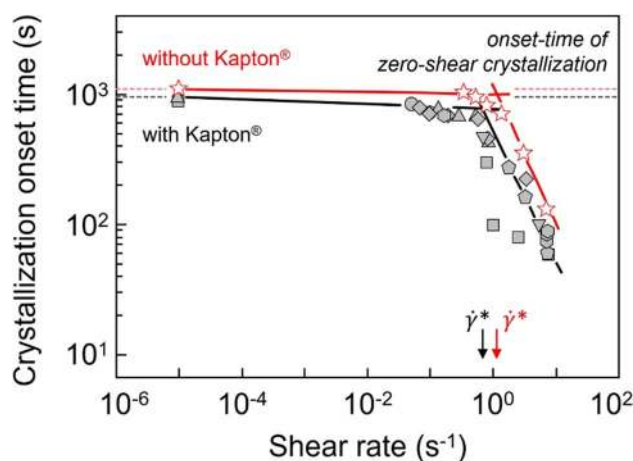


Fig. 3 Crystallization onset times as a function of shear rate of PA 11 samples prepared with and without using Kapton® films (black symbols and red stars, respectively). The crystallization onset times of non-sheared samples are indicated with the corresponding black and red dashed lines, respectively

rates higher than about 0.5 s^{-1} due to formation of additional crystal nuclei. A critical shear rate of around 0.8 to 1 s^{-1} is determined from the intersection of the extrapolated crystallization onset time of the non-sheared samples, and linear fit of onset times observed well above the shear rates where the downturn of the crystallization onset time occurs (Seo et al. 2018)

Figure 4 presents a photograph (left) and POM image (right) of a disk prepared using a shear rate of 7.6 s^{-1} . The images were taken at room temperature after completion of crystallization at $180 \text{ }^\circ\text{C}$ for 1 h. The inner part of the disk in the photograph, where low shear rates are evident, is opaque. In contrast, at large distance from the center, the film appears translucent, with a rather sharp transition from opaque to translucent at a specific radius-value. The change of the optical appearance is interpreted in terms of a critical shear rate, above which crystallization occurs in a different mode. As will be shown below, the crystallinity is independent of the position in the samples, and therefore, the different optical appearance is assumed to be caused by different crystal size and/or superstructure. The POM image at the right-hand side of Fig. 4 additionally reveals with the observed Maltese cross the information that there is orientation of either macromolecules in the amorphous phase and/or of crystals, with the latter described below.

Figure 5 shows micrographs of PA 11 samples taken at room temperature, after shearing the melt at different rates and subsequent isothermal crystallization at $180 \text{ }^\circ\text{C}$ for 1 h. The samples were cut along the radius, from the center to the edge of the disks. Therefore, the flow direction is perpendicular to the cut sections. Higher-magnification micrographs of the sample near the edge of non-sheared and sheared PA 11 (7.6 s^{-1}) are shown to the right in the figure, with the top and bottom images, respectively.

Regarding the images illustrating the structure from the center to the edge (left), the non-sheared sample is shown at the top, while the other images represent the structure

of samples subjected to shear flow before crystallization, with the shear rates indicated at the right-hand side of each thin section. The non-sheared sample shows a space-filled spherulitic structure, with the diameter of the spherulites being $20\text{--}30 \text{ }\mu\text{m}$ (see also right top image), regardless of the position in the disk. In contrast, the sheared PA 11 samples show a gradient structure from the center to the edge due to the increasing shear rates. A critical shear rate for shear-induced formation of nuclei is specified at the position where a distinct change of the semicrystalline superstructure is observed, indicated by yellow circles. The POM micrographs of Fig. 5 confirm consistently in all experiments involving different maximum shear rate the increased nuclei number when the shear rate exceeds about 1 s^{-1} . Worth noting, shearing the melt at a rate above the critical value leads to a tremendous increase of point-like nuclei as well as formation of aligned nuclei as revealed with the bottom-right image.

DSC first-heating scans, measured with a rate of 20 K min^{-1} , of non-sheared (black) and sheared PA 11 at the center (blue) and edge area (red) of the disks are shown in Fig. 6. The purpose of the experiment was to prove the presence of crystals in the edge region of the sheared sample, since POM cannot provide this information (see Fig. 4). However, the melting-peak temperatures and crystallinities of both samples (sheared and non-sheared) and even at different positions (center and edge area) are similar, being about $190 \text{ }^\circ\text{C}$ and 35%, respectively, regardless of the largely different semicrystalline morphology (see the edge structures in the top and bottom thin sections in Fig. 5). Identical melting temperatures are expected since both samples were crystallized at the same temperature of $180 \text{ }^\circ\text{C}$ until completion of the crystallization process.

Figure 7 presents at the top a POM image of a sample sheared at 7.6 s^{-1} for 60 s including information of sampling WAXS patterns as a function of the radius of the disk from the edge (red circle) to the center (blue circle).

Fig. 4 Photograph (left) and POM image (right) of a PA 11 disk crystallized at $180 \text{ }^\circ\text{C}$ for 1 h after shearing the melt at 7.6 s^{-1} for 60 s, taken at room temperature. The orientation of the polarizers is shown at the top right of the POM image

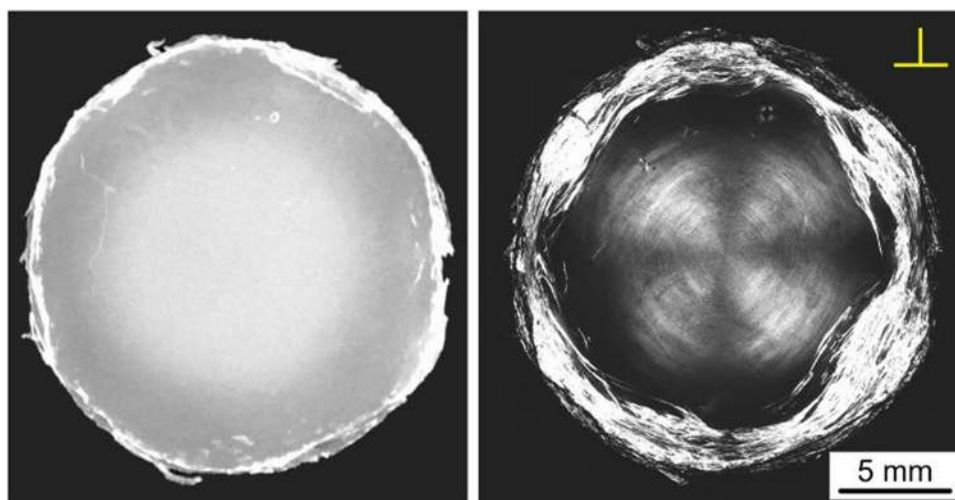
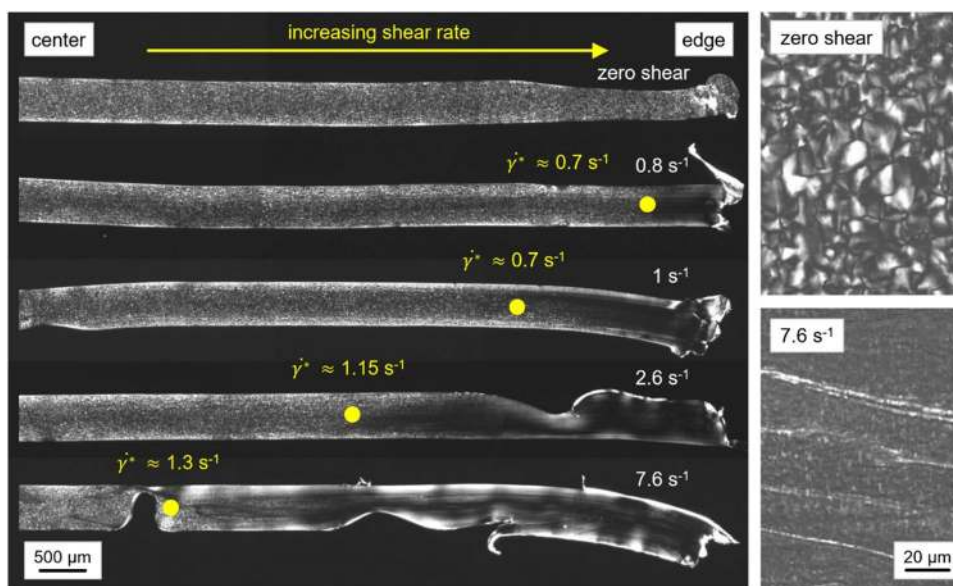


Fig. 5 POM images of PA 11 sections showing the structure from the center to the edge perpendicular to the flow direction, captured at room temperature after shearing the melt at different rates for a constant shear time of 60 s at 190 °C and subsequent isothermal crystallization for 1 h at 180 °C (left). The two images to the right show the structure in the center layer near the edge of non-sheared (top right) and sheared PA 11 (bottom right) at higher magnification



One-dimensional WAXS patterns taken at corresponding positions are shown with the bottom plot in Fig. 7. The scattering patterns collected at the edge and center of the non-sheared sample are indicated with the dashed lines. All samples show three scattering peaks at about 7.4, 20.3, and 23.4 degrees related to the (001), (100), and (010/110) lattice planes, respectively, of the triclinic α -crystals present (Slichter 1959; Kim et al. 1985). As such, the X-ray data consistently confirm that crystallization at 180 °C leads to formation of α -crystals of similar perfection, with the latter indicated by the constant positions of the 100 and 010/110 peaks, regardless of prior shearing.

Figure 8, at the top, shows two-dimensional WAXS patterns in the angular range of the 001 peak of sheared PA

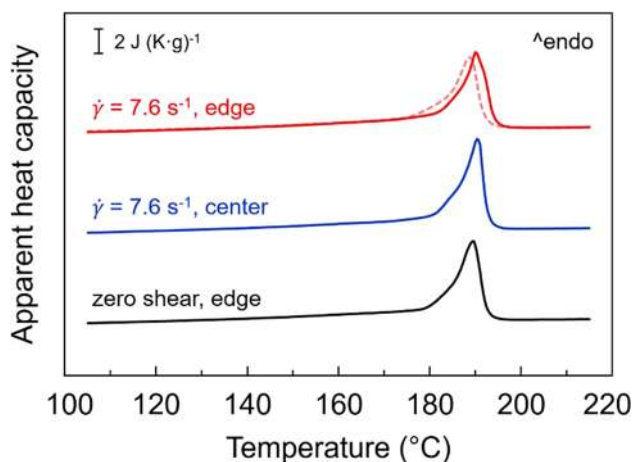


Fig. 6 DSC first-heating scans of non-sheared (black) and sheared PA 11 (blue and red), recorded at 20 K min⁻¹. The red dashed line represents a repetition scan, with the sample taken from a different disk

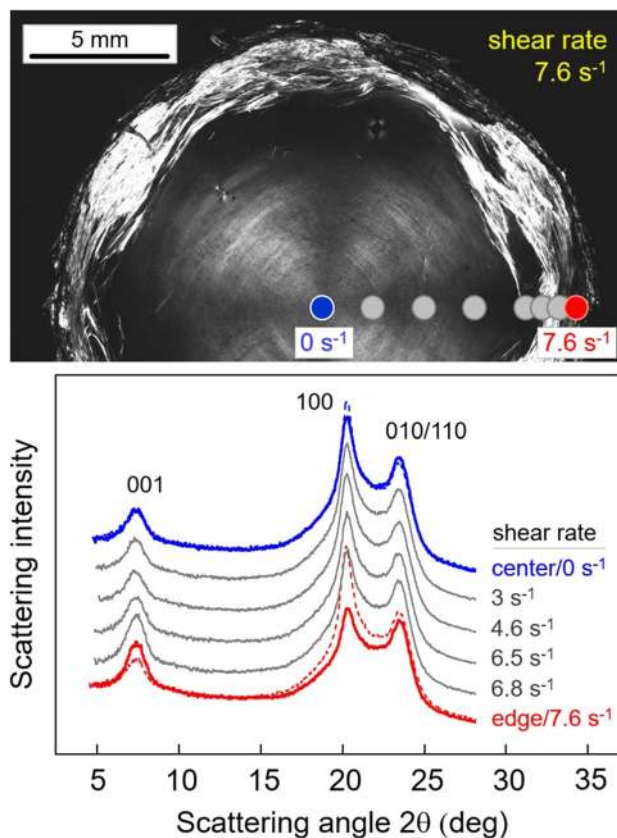


Fig. 7 POM image (top) showing the WAXS-analysis positions from the edge (red) to the center (blue) of the disk, corresponding to different shear rates from 7.6 to 0 s⁻¹, respectively. In the bottom part of the figure are shown WAXS curves taken at the various disk positions with the corresponding shear rates indicated on the right-hand side of the curves. The scattering patterns collected at the edge and center of the non-sheared sample are indicated with the dashed lines

11 (7.6 s^{-1} for 60 s) taken at different distances from the edge (red) to the center of the disk (blue) (see also the POM image in the top part of Fig. 7), while in the bottom plot are shown azimuthal scans of the intensity of the 001 peak. The two-dimensional WAXS patterns served for detection of the crystal orientation along the radius of the sheared disk. Within the analyzed sample plane, the data reveal crystal orientation near the edge, while in the inner part of the disk crystals are randomly oriented. The crystal orientation is clearly detected with the incomplete arc-like Debye-Scherrer ring in the pattern taken at distances lower than 2 mm from the edge. Quantitative information is provided with the azimuthal scans in the bottom plot of Fig. 8, demonstrating, though only weak, increasing crystal orientation toward the edge. Worth noting, despite no crystal orientation was

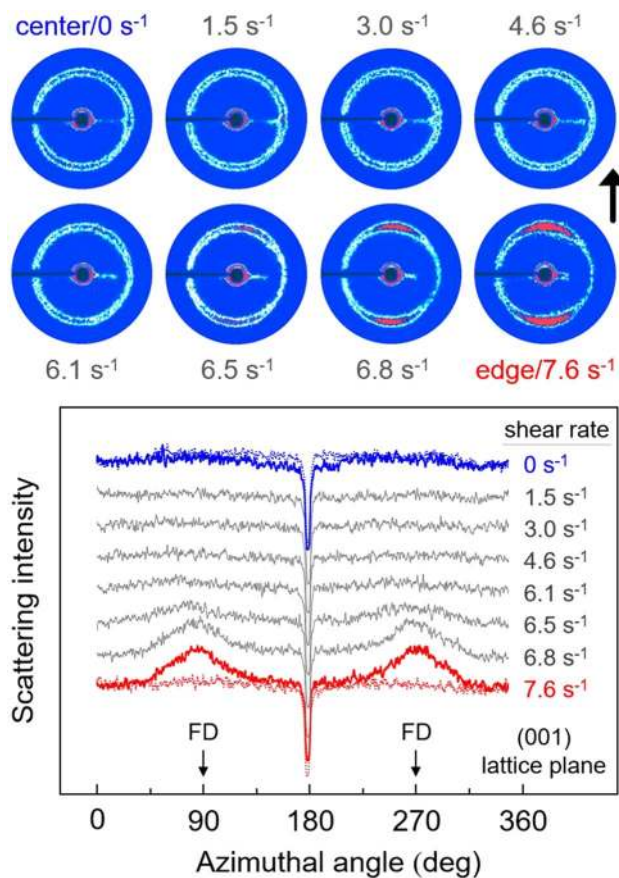


Fig. 8 Two-dimensional scattering patterns in the angular range of the 001-scattering peak of the sheared sample at different positions from the edge to the center of the disk, representing different shear rates (top). The vertical arrow on the right-hand side indicates the flow direction (FD). Scattering intensity as a function of the azimuthal angle at the scattering angle of the 001 peak of the various sample positions (bottom). The data of the non-sheared sample at the edge and center of the disk are presented with the dashed-thin lines. The flow direction (FD) is shown with the arrows at the 90 and 270° positions

detected in the inner part of the disk, the POM image of Fig. 4 (right) revealed with the Maltese cross orientation of molecules which might be related to amorphous-phase orientation, often observed in injection molding or compression molding of amorphous polymers (Rudolph 2009; Meister 2020).

Figure 9 shows POM images of the inner structure of the sheared disk used for WAXS analysis (see Fig. 7). The top image reveals the gradient structure along the radius as discussed above with Fig. 5, while the bottom image shows the structure along the flow direction near the edge, as indicated with the yellow frame in the top image. The yellow circle in the top image emphasizes the radius-position above which there is observed shear-induced crystallization. Note that the observed critical shear rate of 3 s^{-1} of this particular sample is slightly higher than for the samples of Fig. 5, with the mismatch illustrating the uncertainty of the performed experiments. A rough estimation of an average critical shear rate of all samples regardless of the maximum shear rate at the edge reveals a value of $1.4 \pm 0.95 \text{ s}^{-1}$. Again, below this value, there is observed quiescent-like crystallization, while above this value, shear-induced nucleation occurs. If the shear rate is lower than about 5 to 7 s^{-1} , then still spherulitic crystallization is detected, however, with the number of spherulites distinctly increased compared to the center of the disk. In contrast, as demonstrated in the lower image of Fig. 9, at the edge, a qualitatively different morphology evolved, characterized by the presence of long fiber-like objects parallel to the direction of the flow, presumably shish-like structures. Strikingly, only in this part of the sample preferred crystal orientation was measured by WAXS (see Fig. 8).

Regardless of the different morphological features observed as a function of the radius in the sheared disk,

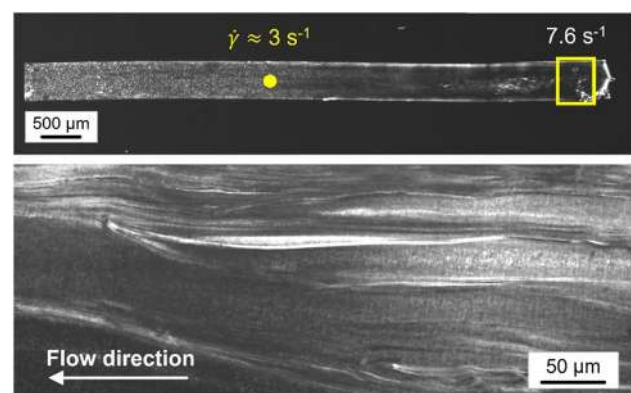


Fig. 9 POM images of sheared PA 11, showing the structure from the center to the edge of the disk (top) and at the edge area (bottom). The direction of flow is perpendicular to the shown section in the top image, while it is indicated with the arrow in the bottom image. The yellow rectangle in the top image illustrates the location represented with the lower image, and the yellow circle indicates the critical shear rate above which the nuclei density increases toward the edge

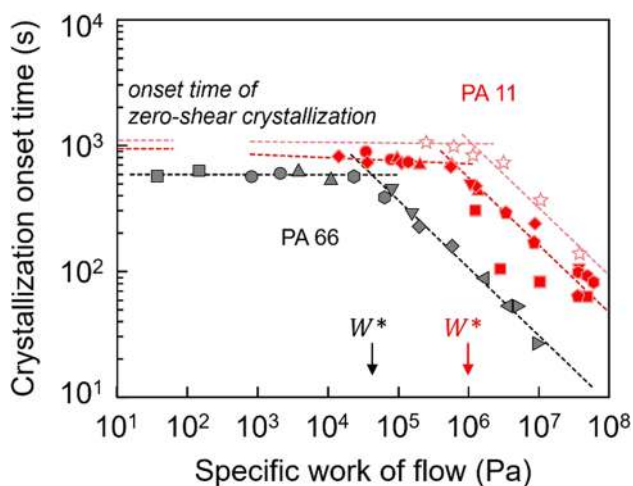


Fig. 10 Crystallization onset time as a function of specific work of flow of PA 11 (red symbols) and PA 66 (black symbols). The data of PA 66 were adapted with permission from Seo et al. 2018, *Macromolecules* 51, 4269–4279. Copyright 2020 American Chemical Society

shearing at rates larger about 1 s^{-1} for 60 s leads to an acceleration of the crystallization process. To accommodate the shearing time, and to permit a comparison with PA 66, crystallization onset times were plotted as a function of the specific work of flow in Fig. 10.

For PA 11 (red symbols), the specific work of flow was calculated from Eq. 1, with the viscosity determined as an average value during the shearing step of the experiments, as proposed in the literature (Mykhaylyk et al. 2008). Information about the specific work of flow of PA 66 (black symbols) was gained from the literature (Seo et al. 2018). The PA 11 samples, collected in this work with (filled symbols) and without using Kapton® films (open-star symbols), show a critical specific work of flow of around 1 MPa (see red arrow marked W^*). In contrast, the critical value above which shear-induced nucleation occurs in PA 66 is only about 0.05 MPa (see black arrow), which is distinctly lower than observed for PA 11. In other words, PA 11 requires more work/energy to generate crystal nuclei by shear. We assume that the higher critical specific work of flow is related to the structure of the repeat unit in the chains, that is, the longer aliphatic sequence in PA 11 and lower hydrogen bond density, as these parameters probably affect relaxation times, being important for the stability of shear-induced formed nuclei. The molar mass of both polymers used for the investigations is very similar (17.2 and 22.3 kg mol^{-1} for PA 11 and PA 66, respectively), with both grades having a polydispersity of 2. As such, the different critical specific works of flow cannot be explained by different chain lengths.

Conclusions

In polymer-manufacturing processes such as extrusion or injection molding, crystallization may be induced by normal and shear forces/stress, causing deformation and/or orientation of the molecules in the melt. These features play an important role for shear-induced crystallization implying a possibility to control or tailor the final structure and eventually the properties. Therefore, in the present work, shear-induced formation of nuclei of PA 11 was analyzed using a conventional parallel-plate rheometer. Crystallization of PA 11 after shearing the melt at different rates for 60 s was followed by the evolution of the viscosity. The critical shear rate and specific work of flow above which shear-induced nucleation occurs are around $1\text{--}2 \text{ s}^{-1}$ and 1 MPa, respectively.

Optical microscopy revealed the gradient structure of the sheared disks along the radius, from the center to the edge, identifying ranges of quiescent-like spherulitic crystallization, spherulitic crystallization starting from additional point-like nuclei which were generated by shear, and shear-induced formation of fibrillar structures. WAXS analysis revealed the presence of oriented crystals only in the range of fibrillar crystallization.

This study quantifies for the first time shear-induced crystal nucleation in PA 11 and allows an initial comparison with PA 66. In case of PA 11, the critical specific work of flow is much larger than in case of PA 66, which must be attributed to the different chemical structure, presumably affecting the orientability of molecular segments in the melt and relaxation times. Regarding these parameters, information is not yet available, suggesting further research efforts for explaining the different behaviors of polymers belonging to the polyamide family.

Funding Open Access funding enabled and organized by Projekt DEAL. KJ and RA received financial support from the European Structural and Investment Funds (ESF). This work was supported by the National Science Foundation under grant no. 1653629.

Open Access This article is licensed under a Creative Commons Attribution 4.0 International License, which permits use, sharing, adaptation, distribution and reproduction in any medium or format, as long as you give appropriate credit to the original author(s) and the source, provide a link to the Creative Commons licence, and indicate if changes were made. The images or other third party material in this article are included in the article's Creative Commons licence, unless indicated otherwise in a credit line to the material. If material is not included in the article's Creative Commons licence and your intended use is not permitted by statutory regulation or exceeds the permitted use, you will need to obtain permission directly from the copyright holder. To view a copy of this licence, visit <http://creativecommons.org/licenses/by/4.0/>.

References

- Acierno S, Puyvelde PV (2005) Effect of short chain branching upon the crystallization of model polyamides-11. *Polymer* 46:10331–10338. <https://doi.org/10.1016/j.polymer.2005.07.097>
- Arkema (2020) Polyamide material database. <https://www.extrematerials-arkema.com/en/materials-database/polyamide-material-database/>. Accessed 22 Sep 2020
- Azzurri F, Flores A, Alfonso GC et al (2003) Polymorphism of isotactic polybutene-1 as revealed by microindentation hardness. Part II: correlations to microstructure. *Polymer* 44:1641–1645 [https://doi.org/10.1016/S0032-3861\(02\)00864-9](https://doi.org/10.1016/S0032-3861(02)00864-9)
- Bello JO, Wood RJK (2005) Micro-abrasion of filled and unfilled polyamide 11 coatings. *Wear* 258:294–302. <https://doi.org/10.1016/j.wear.2004.08.008>
- Brill R (1942) Über das Verhalten von Polyamiden beim Erhitzen. *J Für Prakt Chem* 161:49–64. <https://doi.org/10.1002/prac.19421610104>
- Coppola S, Grizzuti N, Maffettone PL (2001) Microrheological modeling of flow-induced crystallization. *Macromolecules* 34:5030–5036. <https://doi.org/10.1021/ma010275e>
- De Santis F, Pantani R, Titomanlio G (2016) Effect of shear flow on spherulitic growth and nucleation rates of polypropylene. *Polymer* 90:102–110. <https://doi.org/10.1016/j.polymer.2016.02.059>
- Dencheva N, Denchev Z, Oliveira MJ, Funari SS (2007) Relationship between crystalline structure and mechanical behavior in isotropic and oriented polyamide 6. *J Appl Polym Sci* 103:2242–2252. <https://doi.org/10.1002/app.25250>
- Fornes TD, Paul DR (2004) Structure and properties of nanocomposites based on nylon-11 and -12 compared with those based on nylon-6. *Macromolecules* 37:7698–7709. <https://doi.org/10.1021/ma048757o>
- Gadzinowska K, Piorkowska E (2003) Influence of sample thickness and surface nucleation on i-PP crystallization kinetics in DSC measurements. *Polimery* 48:790–799. <https://doi.org/10.14314/polimery.2003.790>
- Genas M (1962) Rilsan (Polyamid 11), Synthese und Eigenschaften. *Angew Chem* 74:535–540. <https://doi.org/10.1002/ange.19620741504>
- Gohn AM, Rhoades AM, Okonski D, Androsch R (2018) Effect of melt-memory on the crystal polymorphism in molded isotactic polypropylene. *Macromol Mater Eng* 303:1800148. <https://doi.org/10.1002/mame.201800148>
- Hadinata C, Gabriel C, Ruellmann M et al (2006) Shear-induced crystallization of PB-1 up to processing-relevant shear rates. *Rheol Acta* 45:539–546. <https://doi.org/10.1007/s00397-005-0057-z>
- Halim KAA, Farrell JB, Kennedy JE (2013) Preparation and characterization of polyamide 11/montmorillonite (MMT) nanocomposites for use in angioplasty balloon applications. *Mater Chem Phys* 143:336–348. <https://doi.org/10.1016/j.matchemphys.2013.09.007>
- Iqbal N, Jariyavidyanont K, Rhoades AM, Androsch R (2019) Critical specific work of flow for shear-induced formation of crystal nuclei in poly (L-lactic acid). *Polym Cryst* 2:e10073. <https://doi.org/10.1002/pcr2.10073>
- Janeschitz-Kriegl H, Ratajski E, Stadlbauer M (2003) Flow as an effective promoter of nucleation in polymer melts: a quantitative evaluation. *Rheol Acta* 42:355–364. <https://doi.org/10.1007/s00397-002-0247-x>
- Jariyavidyanont K, Schick C, Androsch R (2019) Nucleation-controlled dual semicrystalline morphology of polyamide 11. *Polym Int* 68:263–270. <https://doi.org/10.1002/pi.5606>
- Jariyavidyanont K, Williams JL, Rhoades AM et al (2018) Crystallization of polyamide 11 during injection molding. *Polym Eng Sci* 58:1053–1061. <https://doi.org/10.1002/pen.24665>
- Keller A, Machin MJ (1967) Oriented crystallization in polymers. *J Macromol Sci Part B* 1:41–91. <https://doi.org/10.1080/0022346708212739>
- Kim KG, Newman BA, Scheinbeim JI (1985) Temperature dependence of the crystal structures of nylon 11. *J Polym Sci Polym Phys Ed* 23:2477–2482. <https://doi.org/10.1002/pol.1985.180231206>
- Kohan MI (1995) Chapter 13 Commercial nylon plastics and their applications. In: Kohan MI (ed) *Nylon plastics handbook*. Hanser Publishers, Munich, pp 487–599
- Kolesov I, Mileva D, Androsch R (2014) Mechanical behavior and optical transparency of polyamide 6 of different morphology formed by variation of the pathway of crystallization. *Polym Bull* 71:581–593. <https://doi.org/10.1007/s00289-013-1079-9>
- Koscher E, Fulchiron R (2002) Influence of shear on polypropylene crystallization: morphology development and kinetics. *Polymer* 43:6931–6942. [https://doi.org/10.1016/S0032-3861\(02\)00628-6](https://doi.org/10.1016/S0032-3861(02)00628-6)
- Lellinger D, Floudas G, Alig I (2003) Shear induced crystallization in poly(ϵ -caprolactone): effect of shear rate. *Polymer* 44:5759–5769. [https://doi.org/10.1016/S0032-3861\(03\)00633-5](https://doi.org/10.1016/S0032-3861(03)00633-5)
- Meister S (2020) Influence of part dimension on ageing of injection moulded thermoplastic materials: exemplary studies on amorphous polycarbonate. *Microsyst Technol*. <https://doi.org/10.1007/s00542-020-05020-3>
- Mezger TG (2006) *The rheology handbook: for users of rotational and oscillatory rheometers*. Vincentz Network GmbH & Co KG
- Mollova A, Androsch R, Mileva D et al (2013) Effect of supercooling on crystallization of polyamide 11. *Macromolecules* 46:828–835. <https://doi.org/10.1021/ma302238r>
- Mykhaylyk OO, Chambon P, Graham RS et al (2008) The specific work of flow as a criterion for orientation in polymer crystallization. *Macromolecules* 41:1901–1904. <https://doi.org/10.1021/ma702603v>
- Ogino Y, Fukushima H, Takahashi N et al (2006) Crystallization of isotactic polypropylene under shear flow observed in a wide spatial scale. *Macromolecules* 39:7617–7625. <https://doi.org/10.1021/ma061254t>
- Pantani R, Coccorullo I, Volpe V, Titomanlio G (2010) Shear-induced nucleation and growth in isotactic polypropylene. *Macromolecules* 43:9030–9038. <https://doi.org/10.1021/ma101775h>
- Pepin J, Miri V, Lefebvre J-M (2016) New insights into the Brill transition in polyamide 11 and polyamide 6. *Macromolecules* 49:564–573. <https://doi.org/10.1021/acs.macromol.5b01701>
- Refaa Z, Boutaous M, Siginer DA (2018) PLA crystallization kinetics and morphology development. *Int Polym Process* 33:336–344. <https://doi.org/10.3139/217.3525>
- Rhoades AM, Wonderling N, Schick C, Androsch R (2016) Supercooling-controlled heterogeneous and homogenous crystal nucleation of polyamide 11 and its effect onto the crystal/mesophase polymorphism. *Polymer* 106:29–34. <https://doi.org/10.1016/j.polymer.2016.10.050>
- Rudolph N (2009) *Druckverfestigung amorpher Thermoplaste*. Dissertation, University of Erlangen-Nuremberg
- Schick C, Androsch R (2018) Nucleation-controlled semicrystalline morphology of bulk polymers. *Polym Cryst* 1:e10036. <https://doi.org/10.1002/pcr2.10036>
- Schmidt GF, Stuart HA (1958) Gitterstrukturen mit räumlichen Wasserstoffbrückensystemen und Gitterumwandlungen bei Polyamiden. *Z Für Naturforschung A* 13:222–225. <https://doi.org/10.1515/zna-1958-0308>
- Seo J, Takahashi H, Nazari B et al (2018) Isothermal flow-induced crystallization of polyamide 66 melts. *Macromolecules* 51:4269–4279. <https://doi.org/10.1021/acs.macromol.8b00082>
- Slichter WP (1959) Crystal structures in polyamides made from ω -amino acids. *J Polym Sci* 36:259–266. <https://doi.org/10.1002/pol.1959.1203613020>

- Somani RH, Yang L, Hsiao BS et al (2005) Shear-induced molecular orientation and crystallization in isotactic polypropylene: effects of the deformation rate and strain. *Macromolecules* 38:1244–1255. <https://doi.org/10.1021/ma048285d>
- Spoerer Y, Androsch R, Jehnichen D, Kuehnert I (2020) Process induced skin-core morphology in injection molded polyamide 66. *Polymers* 12:894. <https://doi.org/10.3390/polym12040894>
- Tordjeman Ph, Robert C, Marin G, Gerard P (2001) The effect of α , β crystalline structure on the mechanical properties of polypropylene. *Eur Phys J E* 4:459–465. <https://doi.org/10.1007/s101890170101>
- Zhang C, Hu H, Wang D et al (2005) In situ optical microscope study of the shear-induced crystallization of isotactic polypropylene. *Polymer* 46:8157–8161. <https://doi.org/10.1016/j.polymer.2005.06.074>
- Zhang Q, Mo Z, Liu S, Zhang H (2000) Influence of annealing on structure of nylon 11. *Macromolecules* 33:5999–6005. <https://doi.org/10.1021/ma000298d>

Publisher's note Springer Nature remains neutral with regard to jurisdictional claims in published maps and institutional affiliations.